In-Situ Atomic Scale Studies of the Formation of Epitaxial Pt Nanocrystals on Monolayer Molybdenum Disulfide

Shanshan Wang[1]*, Hidetaka Sawada*[1,2,3]*, Qu Chen*[1]*, Grace G. D. Han*[4]*, Christopher Allen*[1,2]*,*
Angus I. Kirkland[1,2]*, Jamie H. Warner*[1*]

[1]Department of Materials, University of Oxford, Parks Road, Oxford, OX1 3PH,
United Kingdom

[2] Electron Physical Sciences Imaging Centre, Diamond Lightsource Ltd, Harwell Science &
Innovation Campus, Didcot, Oxfordshire, OX11 0DE, United Kingdom

[3] JEOL UK Ltd., Silvercourt, Watchmead, Welwyn Garden City, Herts, AL7 1LT,
United Kingdom.

[4]Department of Materials Science and Engineering, Massachusetts Institute of Technology,
Cambridge, US

*Jamie.warner@materials.ox.ac.uk;

Abstract

Pt-nanocrystal:MoS_2 hybrid materials have promising catalytic properties for hydrogen evolution and understanding their detailed structures at the atomic scale is crucial to further development. Here, we use an *in-situ* heating holder in an aberration corrected transmission electron microscope to study the formation of Pt nanocrystals directly on the surface of monolayer MoS_2 from a precursor on heating to 800^{o}C. Isolated single Pt atoms and small nanoclusters are observed after *in-situ* heating, with two types of preferential alignment between the Pt nanocrystals and the underlying monolayer MoS_2. Strain effects and thickness variations of the ultrasmall Pt nanocrystal supported on MoS_2 are studied, revealing that single atomic planes from a non-layered face-centre cubic bulk Pt configuration with a lattice expansion of 7-10% compared to that of bulk Pt. The Pt nanocrystals are surrounded by an amorphous carbon layer and in some cases have etched the local surrounding MoS_2 material after heating. Electron beam irradiation also initiates Pt nanocrystal etching of the local MoS_2 and we study this process in real time at atomic resolution. These results show that the presence of carbon around the Pt nanocrystals does not affect their epitaxial relationship with the MoS_2 lattice. Single Pt atoms within the carbon layer are also immobilized at high temperature. These results provide important insights into the formation of Pt:MoS_2 hybrid materials.

KEYWORDS: Pt nanocrystals, MoS_2, ADF-STEM, catalysts, *in-situ* heating, etching

Hydrogen production is an important chemical reaction for energy applications such as fuel cells, which utilize metal catalysts.[1–4] The hydrogen evolution reaction is part of the water splitting process for hydrogen production and is a promising 'green' approach for which Pt nanoparticles are the most effective electrochemical catalysts for converting H^+ to H_2.[5,6] MoS_2 has emerged as an alternative to the expensive Pt based catalysts for HER[7–13] and recent results have also shown that a hybrid system of Pt nanocrystals and MoS_2 can increase performance beyond that of MoS_2 alone, with the added benefit of reduced Pt loading compared to traditional Pt-carbon catalytic systems.[14,15]

Prior work has shown that noble metal catalysts, such as Pd and Pt, can be formed directly on the surface of MoS_2 using solution phase chemistry with epitaxial orientations between the lattice of the metal relative to that of the MoS_2.[16] Understanding the atomic level structure of these hybrid systems is critical for building an accurate understanding of their catalytic behaviour. Aberration-corrected transmission electron microscopy (AC-TEM) is able to image atomic structures of these systems and the use of *in-situ* holders enables dynamics and transformations to be capture under different environmental conditions.[17–22] Annular dark field scanning transmission electron microscopy (ADF-STEM) enables the observation of single Pt atoms and other metal dopants on the both surface and substitutional sites in MoS_2.[23–31]

Recent work[27] using ADF-STEM has shown that Pt atoms and nanocrystals adhere strongly to surface bound carbon on MoS_2, influencing the local position of Pt atoms relative to the MoS_2 lattice. In clean MoS_2 areas the single Pt atoms can migrate under electron beam irradiation, but are trapped by S vacancies, leading to a loss of catalytic activity. When a significant number of Pt atoms aggregate to form a cluster, interactions with the MoS_2 surface are likely to be different from those of single atoms. However, studies of Pt nanocrystal:MoS_2 epitaxial correlations using *in-situ* heating holders and complimentary ADF-STEM imaging have not been reported. Here, we utilize an *in-situ* heating holder and ADF-STEM to study structural transformations of suspended monolayer MoS_2 up to 800^{o}C.

Results and Discussion

Figure 1, shows the sample preparation used to deposit a Pt precursor from an ethanol solution followed by air drying. The sample was subsequently first heated from room temperature to 500^{o}C over a 5-minute period and then further to 800^{o}C to track the structure and dynamics of the Pt atoms. An accelerating voltage of 60kV was used for all ADF-STEM imaging to reduce the production of S vacancies and other damage from the electron beam.

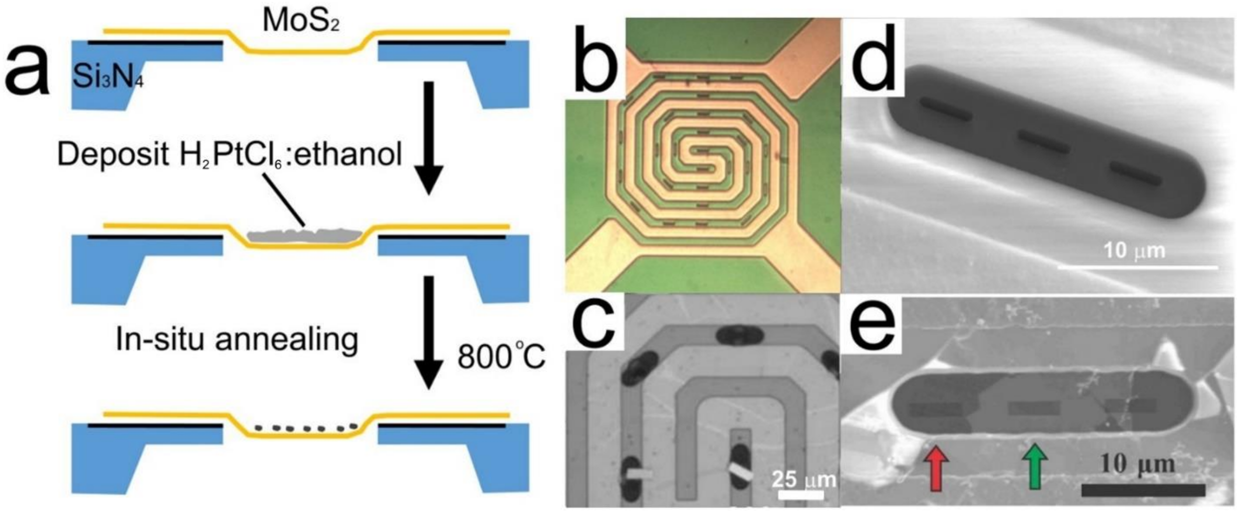

Figure 1. (a) Schematic diagram of Pt deposition on MoS_2 within an in-situ heating holder. (b) Optical microscope image of the *in-situ* heating chip containing thin Si_3N_4 windows and a Pt spiral coil used to heat the sample. (c) SEM of the *in-situ* heating chip showing the oval shaped regions containing the thin Si_3N_4 membrane and the Pt heating coils. (d) SEM image of a thin Si_3N_4 membrane region with three windows cut using FIB. (e) Si_3N_4 window with FIB cut slits after transferring the MoS_2.

Prior to *in-situ* heating, ADF-STEM imaging of the suspended region of the MoS_2 **Figure 2**a, shows preferential aggregation of the Pt precursor in this region. Heating to 500^{o}C, **Figure 2**b, and then to 800^{o}C, **Figure 2**c, results in the formation of Pt nanocrystals. Higher magnification ADF-STEM images show that the Pt nanocrystals are typically a few nanometres in diameter, but also there are a large number of isolated Pt atoms (**Figure 2**d-f). However, the main focus of the research reported here is to understand the fundamental atomic level interactions between the Pt and MoS_2, rather than trying to form ultra-narrow size distributions of nanoparticles.

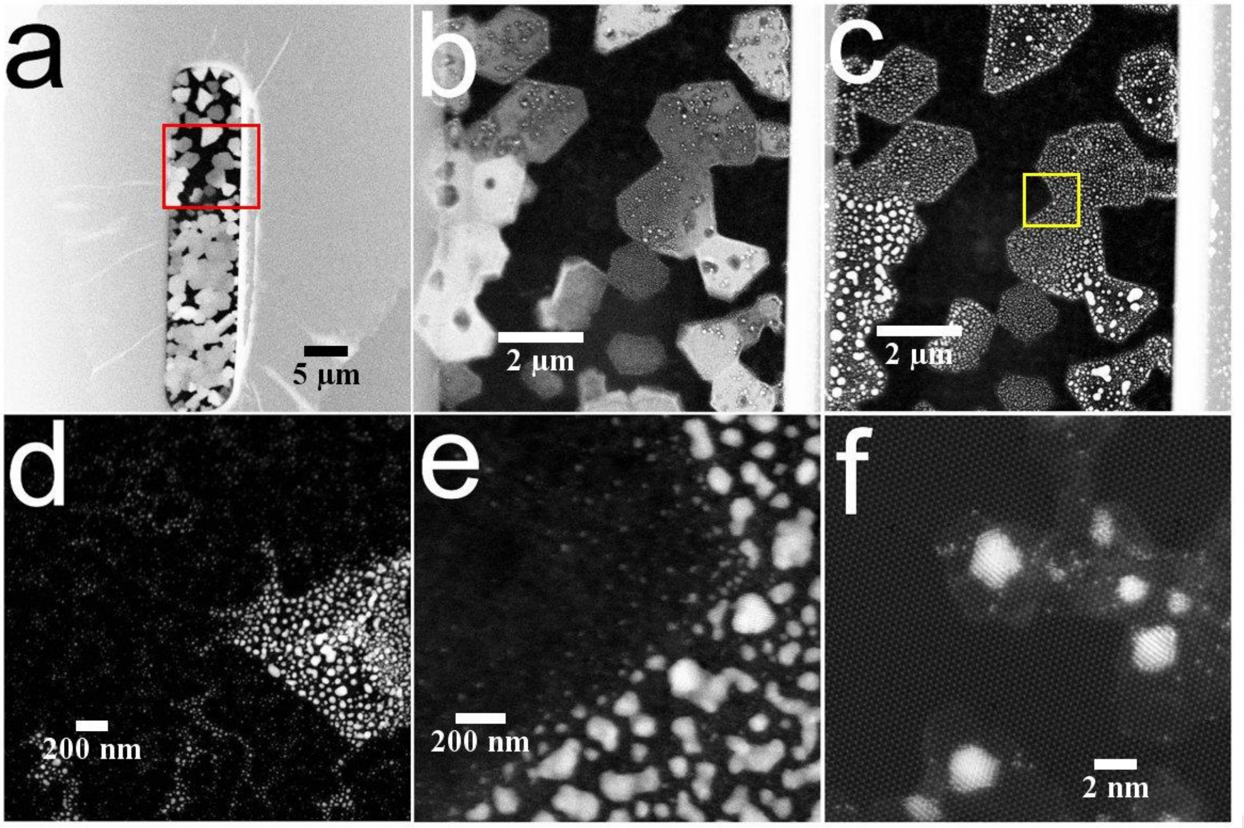

Figure 2. (a) Room temperature low-magnification ADF-STEM image showing the aggregation of Pt material on the surface of MoS_2 within the suspended region. (b) ADF-STEM image of the region marked with the red box in (a) heated to 500^oC. (c) Same region as in (b) but after heating to 800^oC. (d)-(f) ADF-STEM images at different magnifications showing the formation of Pt nanoclusters on MoS_2. Region in (e) is indicated by the yellow box in (c).

After heating to 800^oC, the Pt nanocrystals were crystalline with a high degree of hexagonal faceting and many regions of the MoS_2 surrounding the faceted Pt nanocrystals had been etched away (**Figure 3**). This occurred in regions not been exposed to electron beam irradiation indicating that it is an intrinsic process related to the catalytic effect of the Pt nanocrystals at high temperature. We speculate that the etching could be ascribed to the Pt-catalysed chemical reaction between MoS_2 and gas molecules in the TEM chamber, such as oxygen and hydrogen at high temperature, which may lead to the product of Mo metal and gases such as sulphur dioxide (SO_2) or hydrogen sulphide (H_2S). Mo can coalesce with the Pt particle, supporting our observation of the size increase of the Pt nanocrystal as the etching proceeds, which will be shown in **Figure 7**. The sulphur containing gases will desorb from the surface. The chemical pathways may be quite complex and multi-staged, but the simplistic reaction outcomes can be expressed as follows:

$$MoS_2 + 2O_2 \xrightarrow[800\ ^{o}C]{Pt} Mo + 2SO_2$$

$$MoS_2 + 3O_2 \xrightarrow[800\ ^{o}C]{Pt} Mo + 2SO_3$$

$$MoS_2 + 2H_2 \xrightarrow[800\ ^{o}C]{Pt} Mo + 2H_2S$$

In **Figure 3**a, the orientations of many faceted Pt nanocrystals are aligned, even when the nanocrystals are no longer attached to the MoS_2 and are supported solely by a thin carbon layer, as indicated by the red circle in **Figure 3**b. Using an accelerating voltage of 60kV increases the contrast of this thin carbon layer. A large number of isolated Pt atoms on the surface of MoS_2 are seen across the region (**Figure 3**c) and using false colour (**Figure 3**d) highlights that these are all within a carbon surface layer, even in regions away from the MoS_2. Single Pt atoms were rarely found outside the carbon areas at these high temperatures. In addition, several Pt nanocrystals were still attached to the edge of the MoS_2 and exhibited a slightly different geometry than those either on top of the MoS_2 or supported only by the carbon region. This difference in geometry is due to nanoparticle attachment at the edge of 2D crystals causing deformation during etching to maximize the edge interface contact area. It is worth mentioning that the carbon contamination was unintentionally introduced on the MoS_2 surface likely due to PMMA residue from transfer, the solvent used to deposit the Pt precursor, and the hydrocarbon contamination in the air.

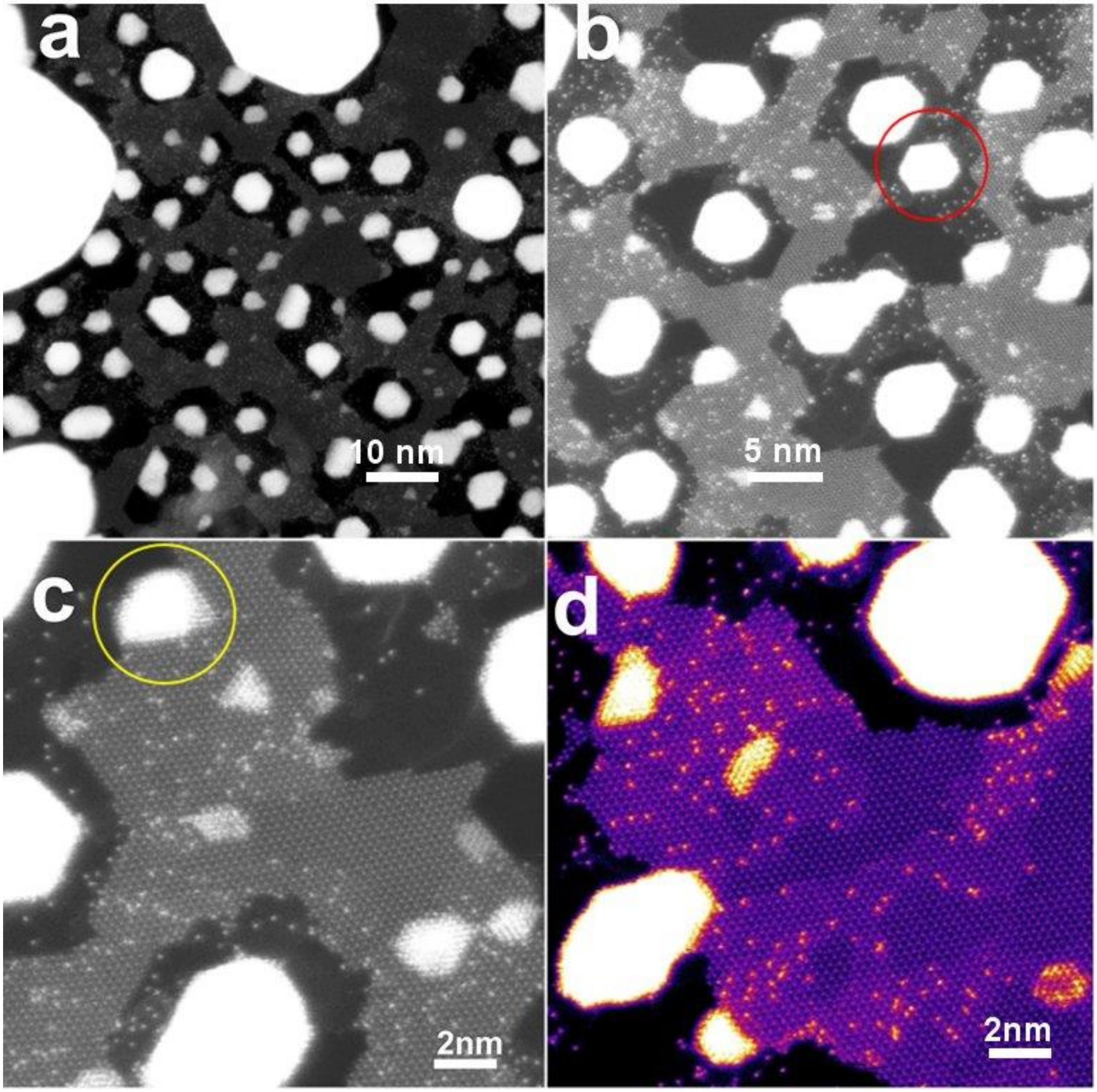

Figure 3. ADF-STEM images showing Pt nanocrystals that have etched their local surrounding MoS_2 region after heating to 800^{o}C. (a)-(c) Different magnification images showing the etched regions. Red circle in (b) shows an aligned Pt nanocrystal supported by only carbon. Yellow circle in (c) shows a Pt nanocrystal attached to the edge of MoS_2. (d) Fire ‘LUT’ used to produce a colour image to highlight the presence of amorphous carbon in areas containing single Pt atoms.

Figure 4a shows an ADF-STEM image of a region containing several Pt nanocrystals with resolved lattice structures together with the power spectrum calculated from the entire image (**Figure 4**b) showing the alignment between the (111) crystal plane from the ensemble of Pt nanocrystals with one zigzag lattice orientation of monolayer MoS_2 (one crystal direction from the {100} crystal plane family of MoS_2 monolayers) as the dominant epitaxial tendency. **Figure 4**c shows a high magnification ADF-STEM image from the region indicated by the yellow box in **Figure 4**a. The Pt nanocrystal is attached to the edge of the MoS_2 and also has the (111) planes aligned with the MoS_2 zigzag lattice direction. Such lattice alignment relationship in the real-space image is also marked by red and yellow lines in **Figure 4**c, representing (111) planes of Pt and MoS_2 zigzag lattice planes, respectively. This demonstrates that even after disconnection from the MoS_2 lattice, the Pt nanocrystals maintain their orientation and that the interaction with the carbon support does not lead to large scale crystal deformations and the loss of the initial epitaxial orientation set by the MoS_2. The interplanar spacing of the (111) crystal plane of Pt can be calculated using MoS_2 lattice as the reference, yielding a value of ~2.28 Å, which is very close to that for the bulk Pt (2.265 Å), indicating no obvious strain effect in the Pt nanocrystal of this scale on MoS_2. **Figure 4**e shows another individual hexagonal shaped Pt nanocrystal fully supported on the MoS_2 surface, which displays the same epitaxial relation between Pt and MoS_2, as evidenced by the FFT analysis in **Figure 4**f. The d-spacing of the (111) plane of Pt is ~2.27 Å, consistent with that of both the Pt nanocrystal attached on the MoS_2 edge and the bulk Pt, indicating little impact from the monolayer MoS_2 substrate on the lattice configuration of Pt nanocrystals locating above.

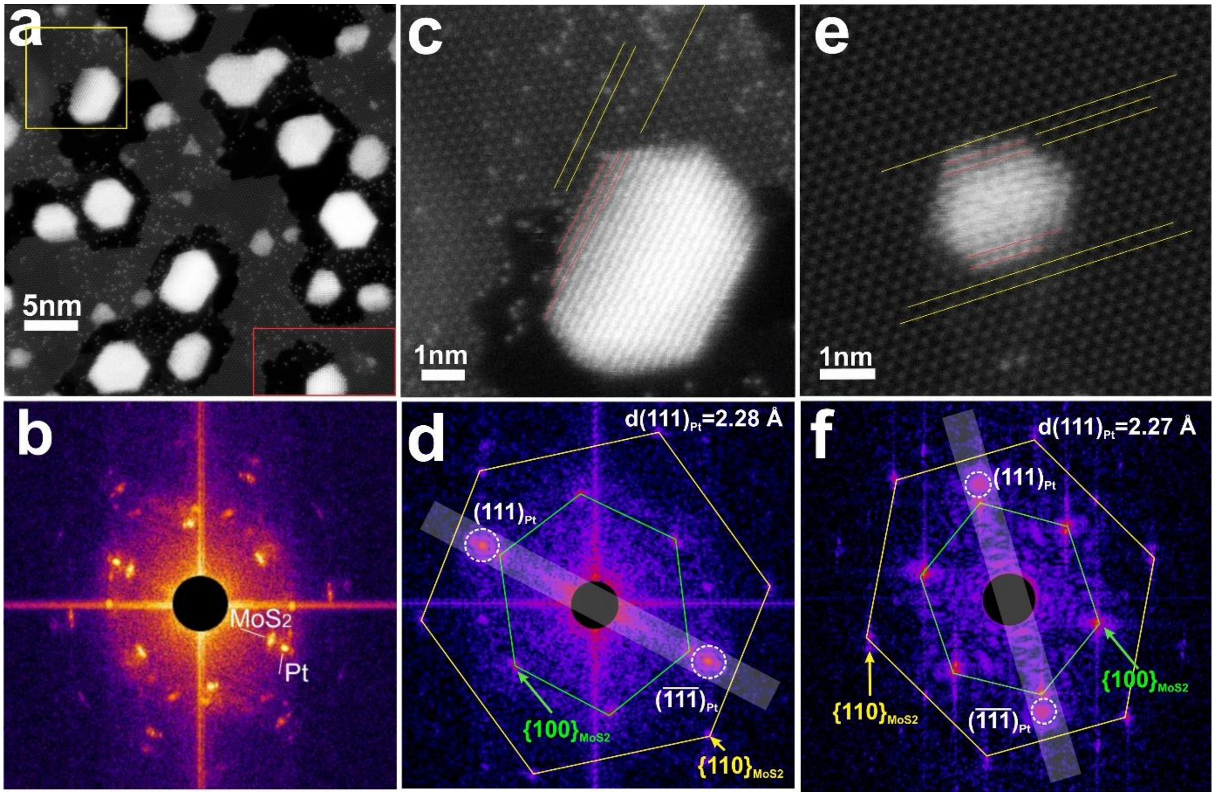

Figure 4. ADF-STEM images showing large scale epitaxial correlations between Pt and MoS_2. Temperature is 800°C. (a) Image of a region containing several Pt nanocrystals. (b) Power spectrum calculated from (a) showing alignment of the Pt nanocrystals with the MoS_2 lattice. A black circle has been used to mask the central peak to improve visualization. (c) ADF-STEM image showing a Pt nanocrystal attached to the edge of MoS_2 corresponding to the yellow boxed region indicated in (a). (d) FFT of (c) with reflexes from both MoS_2 and Pt labelled. (e) ADF-STEM image showing a Pt nanocrystal attached on the monolayer MoS_2 surface. (f) FFT of (e).

In addition to the epitaxial relation discussed in **Figure 4**, the Pt nanocrystal can orient along other lattice directions of monolayer MoS_2. **Figure 5**a is a high magnification ADF-STEM image from the region marked by the red box in **Figure 4**a with its FFT images corresponding to the yellow and red boxed region shown in **Figure 5**b and c, unveiling the lattice information in the reciprocal space for Pt and MoS_2, respectively. Both the reflection spots and the zone axis are labelled. Based on the distance between each reflection spot to the central spot, indicating the lattice spacing, and the intersection angle between reflexes, correlating with the interfacial angle, in **Figure 5**b, it can be found that the Pt nanocrystal is imaged along the $[1\bar{1}0]$ zone axis, giving reflections corresponding to the lattice planes of (111), $(1\bar{1}1)$ and (002) as three closest reflexes to the central spot. It is worth noting that the reflection pattern of the Pt nanocrystal is not a regular hexagon. The (111) and $(1\bar{1}1)$ planes are both close packed planes with the same lattice periodicity, and the interfacial angle between them is measured to be ~110°, while the (002) plane adopts a different atom arrangement manner and the intersection angle between (002) and (111) plane is ~54.1°. The atomic model of the Pt crystal corresponding to the FFT in **Figure 5**b is shown in **Figure 5**e with its unit cell model shown in **Figure 5**d, adopting a face-centred cubic (FCC) structure. Both the angle between corresponding lattice planes and the lattice spacing in **Figure 5**b agree well with the pristine bulk Pt model in **Figure 5**e. **Figure 5**f is the FFT of the entire region of **Figure 5**a. It shows that the (002) plane of Pt aligns with one armchair direction of monolayer MoS_2 (one lattice orientation in the {110} crystal plane family of MoS_2), highlighted by the white column labelled '1'. Since the intersection angle between (002) and (111) plane of Pt is close to 60°, which is the smallest angle between two armchair directions of monolayer MoS_2, the (111) plane of Pt also roughly aligns with another armchair direction of MoS_2 with an angle mismatch of < 5°, indicated by the white column labelled '2'. Such an epitaxial relation between Pt and MoS_2 can be expressed as $(001)_{MoS2}$ // $(1\bar{1}0)_{Pt}$, $[110]_{MoS2}$ // $[002]_{Pt}$. The lattice spacing corresponding to {111} and (002) of Pt are measured to be 2.27Å and 1.91Å, respectively, consistent with bulk Pt well, indicating that this type of epitaxy between the Pt nanocrystal and monolayer MoS_2 also does not trigger a predominant lattice deformation for Pt nanocrystals. The crystallographic relationship between Pt and MoS_2 in the real space confirms the conclusion obtained in the reciprocal space (**Figure 5**g), showing (002) and (111) planes of Pt being parallel with two armchair directions of monolayer MoS_2, respectively, marked by solid and dashed lines.

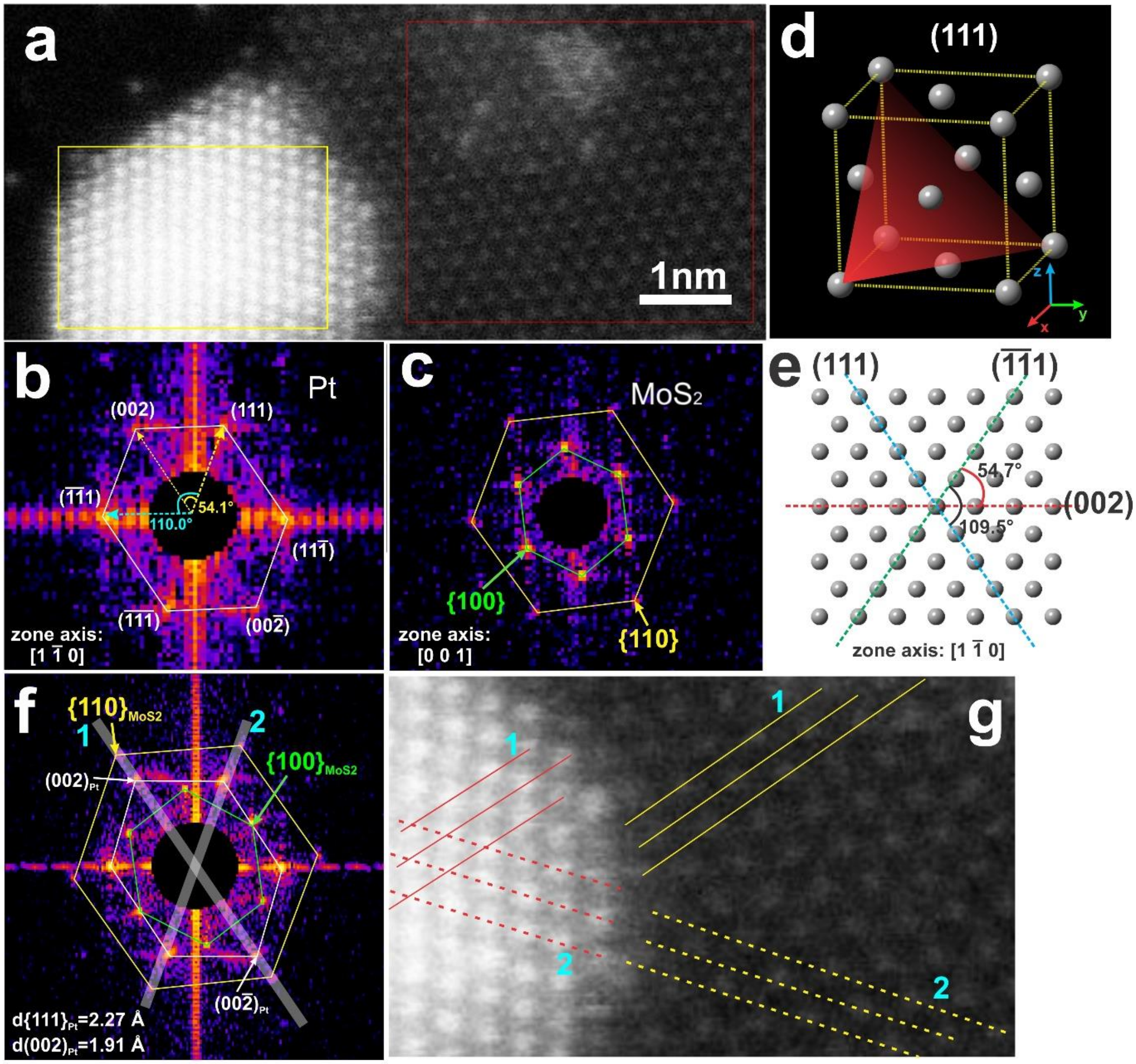

Figure 5. ADF-STEM image of a Pt nanocrystal attached to the edge of MoS_2 monolayer, corresponding to the red boxed region in **Figure 4**a. Two boxed regions are used for the FFT presented in (b) yellow box and (c) red box, respectively. (d) Unit cell of the FCC Pt crystal, with the (111) lattice plane highlighted in red. (e) Atomic model of the Pt crystal corresponding to the

FFT in (b). (f) FFT from the entire ADF-STEM image in (a). (e) Magnified ADF-STEM image of the interface region between Pt nanocrystal and MoS_2 with lines indicating the aligned lattice directions with red for Pt and yellow for MoS_2. Solid lines correspond to the lattice plane alignment between (002) plane of Pt and one MoS_2 armchair direction, while dashed lines correspond to the alignment between (111) plane of Pt and another MoS_2 armchair direction.

For those Pt nanocrystals with an ultrasmall size consisting of approximately 20 atomic columns in projection supported on the monolayer MoS_2 surface (**Figure 6**a, d), the prevalent epitaxial orientation of Pt on MoS_2 is to have two directions belonging to the {111} crystal plane family of Pt aligned with two zigzag directions of MoS_2, respectively, with an angle mismatch of <5°. The zone axis is $[1\bar{1}0]$. Such lattice alignment relation can be expressed as $(001)_{MoS2}$ // $(1\bar{1}0)_{Pt}$, $[100]_{MoS2}$ // $[111]_{Pt.}$ and is confirmed by **Figure 6**b, c and **Figure 6**g, h. **Figure 6**b is the FFT of the entire region of **Figure 6**a, while **Figure 6**c is the FFT of the Pt nanocrystal labelled in the red box of the inset on the bottom right of **Figure 6**a. Four reflexes in **Figure 6**b can be assigned to two lattice directions corresponding to the {111} crystal plane family of Pt, having an interplanar spacing of ~2.44Å and an interfacial angle of ~ 68°. The Pt lattice spacing has an expansion of ~ 7.7% compared to the bulk Pt and becomes closer to the zigzag lattice spacing of monolayer of MoS_2 (~ 2.7Å). This can be confirmed by **Figure 4**d, e, where reflection spots corresponding to (111) or $(11\bar{1})$ plane of Pt and the MoS_2 zigzag lattice direction almost merge together, which shows an obvious difference from FFT images in **Figure 4**, in which these reflexes are clearly separated. In addition, the reflexes of Pt changes from sharp spots shown in **Figure 4** to blurry ones with an increased size, indicating a growing level of the structural disorder, which may include a broader distribution of the lattice spacing and orientation. The enhanced lattice distortion in Pt could be attributed to two potential reasons. One derives from the impact of the rigid monolayer MoS_2 lattice on the supported Pt nanocrystal, which possesses an ultrasmall thickness and a relatively high ductility as the nature of metal, making it easy to deform in order to match the periodicity of the MoS_2 template better. The other reason could come from the influence of the electron beam irradiation, which supplies energy to increase the random atom displacement in this ultrasmall Pt nanoparticle. Reflexes corresponding to (002) planes of Pt can hardly be detected in **Figure 6**c, which might be due to a low intensity of this reflection spot compared with those from {111} lattice plane family of Pt. FFT images corresponding to different regions of **Figure 6**f shows a similar trend as what has been discussed for **Figure 6**a (**Figure 6**g-j). The interplanar spacing of {111} crystal plane family of Pt is measured to be ~ 2.48Å, having an expansion of ~9.5% compared to that of bulk Pt crystal. Figure 3k is the atomic model of **Figure 6**a with the corresponding multislice ADF-STEM image simulation shown in **Figure 6**l. To determine the thickness of the Pt nanocrystal, we compare the relative intensity variation between the single Mo columns in monolayer MoS_2 (marked in yellow dashed boxes in the inset on the left bottom of **Figure 6**a and **Figure 6**l) and the Pt columns in the Pt/MoS_2 epitaxial region (marked in cyan dashed boxes in **Figure 6**a and **Figure 6**l) for both the experimental ADF-STEM image and the image simulations with different Pt thickness (**Figure 6**m) using a previously reported method.[32] It is worth noting that the pristine monolayer MoS_2 lattice chosen for the intensity measurement is not close to the Pt nanocrystal in **Figure 6**a because these regions are contaminated by hydrocarbon contamination. Instead, a region absent of contamination coverage was selected, which is in the same image of **Figure 6**a, as shown by the inset on the left bottom of **Figure 6**a. It is confirmed that the Pt nanocrystal is two-atom-thick, having only one Pt atom in each atomic column locating either in the first or the second layer due to the non-planar FCC structure of the Pt crystal, as shown by the projection and side view of the epitaxial structure in **Figure 6**k and the 3D view of this model in **Figure 6**n.

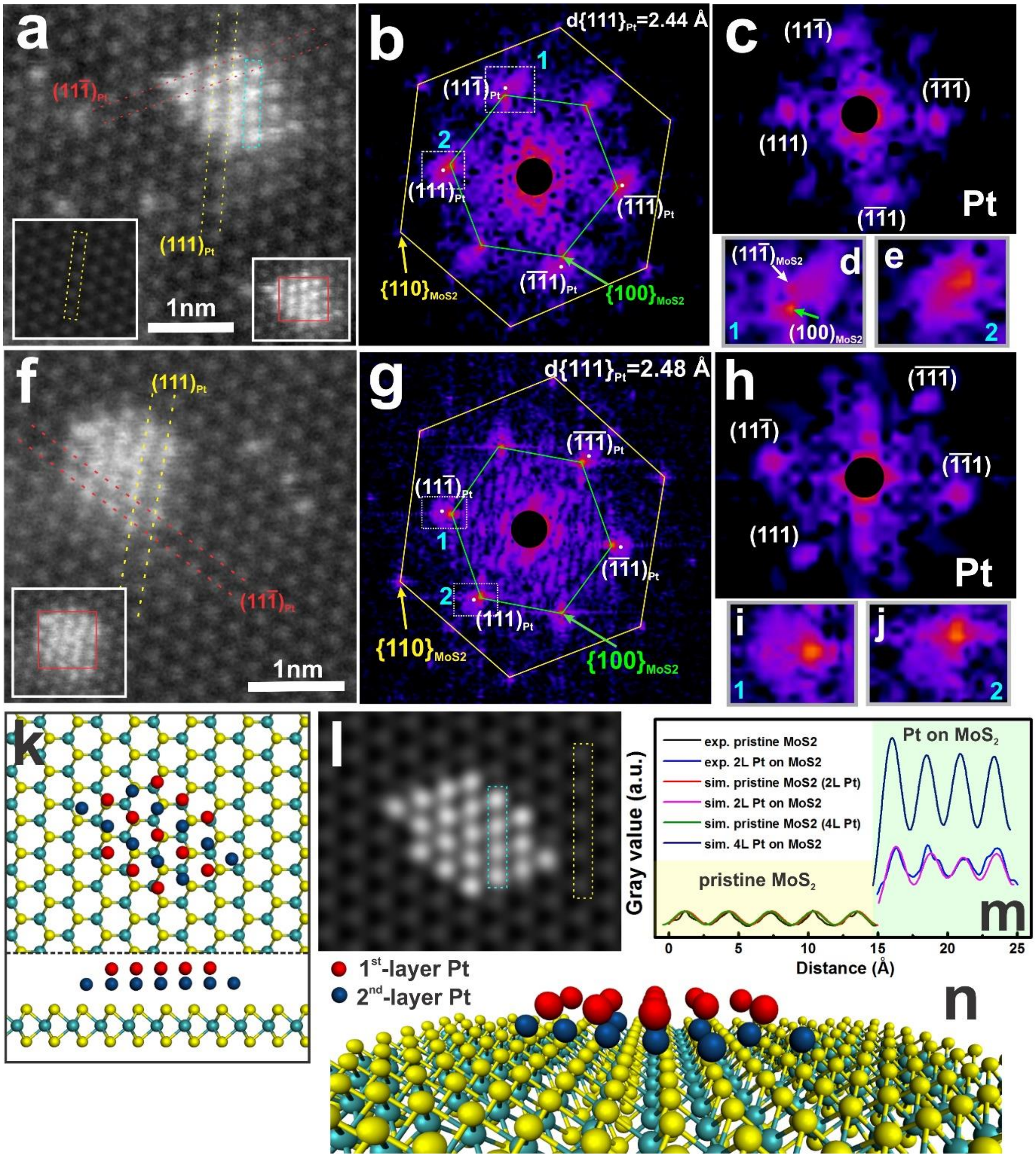

Figure 6. (a) ADF-STEM image of an ultrasmall Pt nanocrystal epitaxially orientated on monolayer MoS$_2$. Inset on the left bottom shows a clean region of MoS$_2$ used for the intensity

measurement on single Mo atomic columns for the experimental image in (m). (b) FFT of the entire region of (a). (c) FFT of the Pt nanocrystal marked in the red box in the inset on the right bottom of (a). (d,e) Zoomed-in images of regions in white boxes labelled '1' and '2', respectively, in (b). (f) ADF-STEM image showing another example of an epitaxially orientated ultrasmall Pt nanocrystal on monolayer MoS_2. (g) FFT of the entire region of (f). (h) FFT of the Pt nanocrystal marked in the red box in the inset on the left bottom of (f). (i,j) Zoomed-in images of regions in white boxes labelled '1' and '2', respectively, in (g). (k) Atomic model of (a). The first and second layer of Pt atoms are in red and blue, respectively. (l) Multislice ADF-STEM image simulation corresponding to the atomic model in (k). (m) Line profiles comparing the atomic column intensities from the experimental and simulated images. (n) 3D perspective side view of the model in (k).

Further insights into the etching of MoS_2 by the Pt nanocrystals can be gained by using the electron beam to supply energy and initiate the process (**Figure 7**). **Figure 7**a shows an ADF-STEM image of the sample following heating at 800^{o}C for 3 hours. The amount of amorphous carbon has been reduced, leaving cleaner regions of MoS_2. The presence of the small amount of carbon still at 800C is due to its increased graphitization from the Pt material. A high magnification ADF-STEM image (**Figure 7**b) shows a faceted Pt nanocrystal supported directly on MoS_2, which starts to catalytically etch the surrounding MoS_2 (**Figure 7**c-h), initiated by exposure to the electron beam. As the Pt nanocrystal starts etching, a small carbon disk becomes visible (orange arrow in **Figure 7**e) indicating that the Pt is still not free from the amorphous carbon material. The shape of the Pt nanocrystal changes as it interacts with the MoS_2 edge during the etching process. The integration time during ADF-STEM imaging in **Figure 7** was sufficiently long to enable visualization of the carbon disk, but this caused the ADF-STEM signal from the Pt lattice to saturate. **Figure 8** shows another example of this behaviour in which the Pt nanocrystal deformation is evident (**Figure 8**f) and strong epitaxial alignment is observed. Comparison of the Pt nanocrystal before and after etching shows an increase in size that is likely due to the incorporation of Mo atoms.

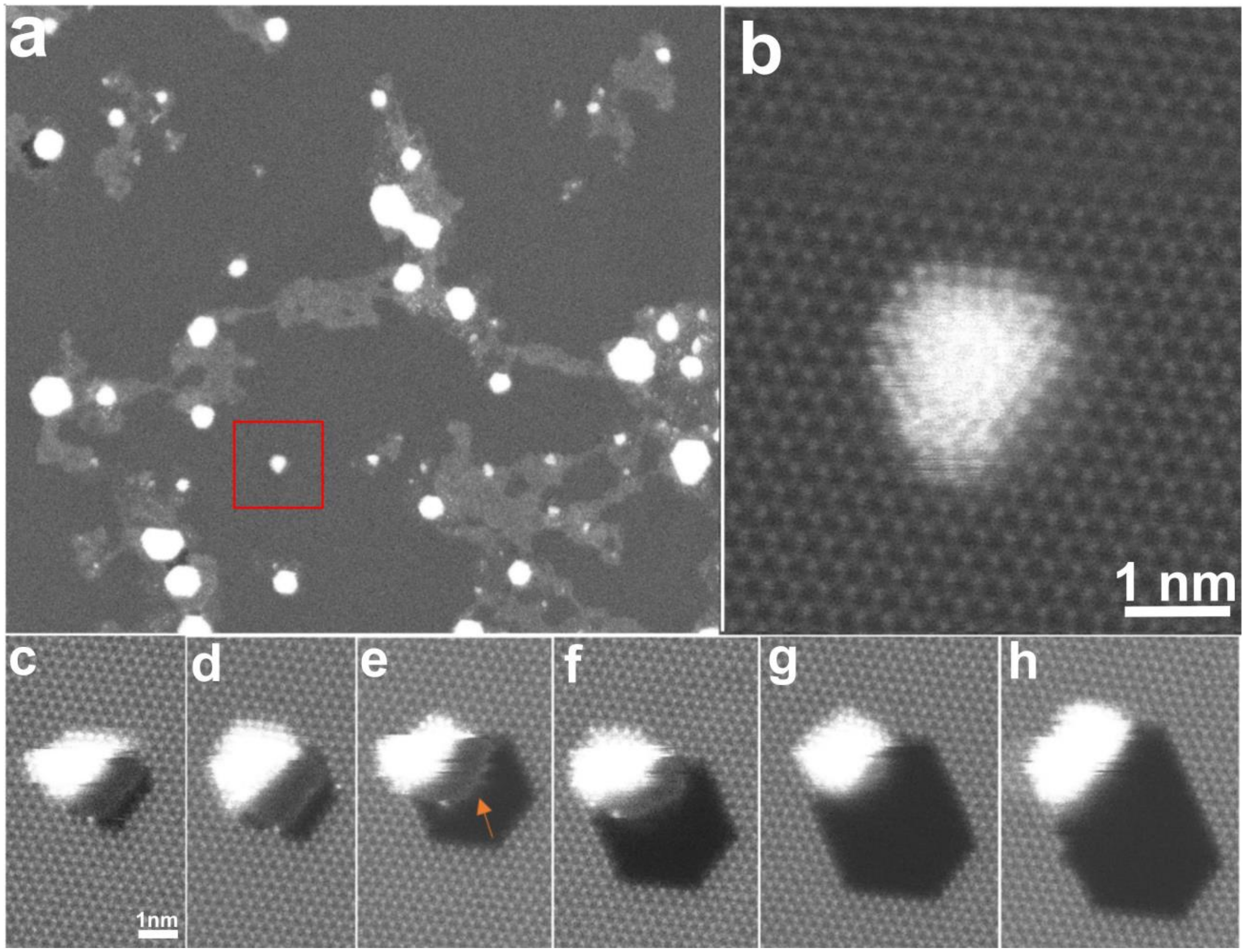

Figure 7. *In-situ* etching of MoS_2 by Pt nanocrystals, driven by electron beam irradiation. Temperature is 800°C. (a) ADF-STEM image of a region after 3 hours at 800°C showing reduced carbon and Pt nanocrystals. (b) ADF-STEM image corresponding to the red boxed region in (a), showing a faceted Pt nanocrystal supported on MoS_2. (c)-(h) Sequence of ADF-STEM images showing catalytic etching of MoS_2 by the Pt nanocrystal in (b), initiated by electron beam irradiation. Orange arrow indicates an amorphous carbon disk. Time between frames is ~30s.

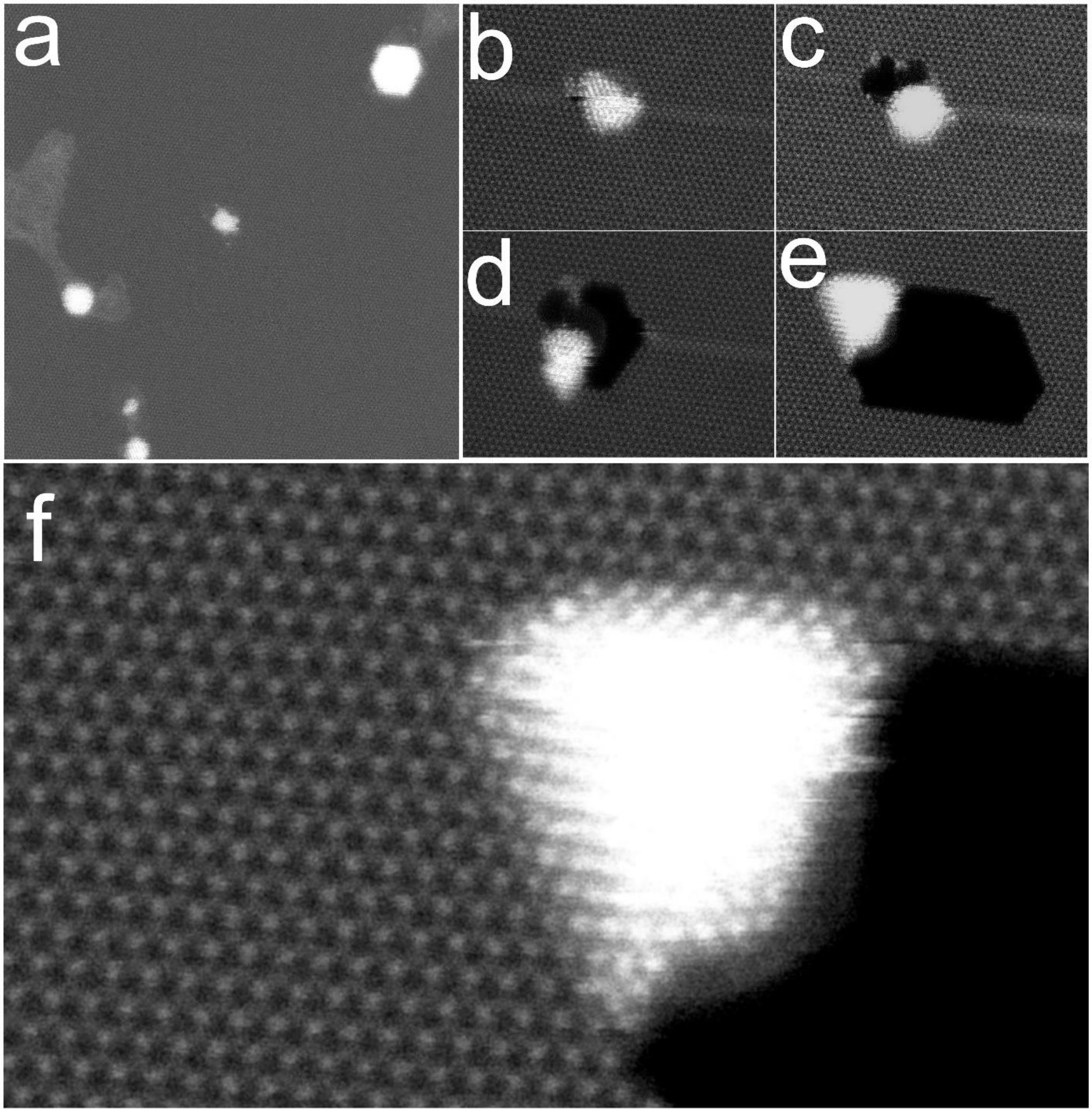

Figure 8. A further example of *in-situ* etching of MoS_2 by Pt nanocrystals, driven by electron beam irradiation. Temperature is $800^{o}C$. (a) ADF-STEM image of a region after 3 hours at $800^{o}C$ showing reduced carbon and an isolated Pt nanocrystal. (b)-(e) Sequence of ADF-STEM images showing catalytic etching of MoS_2 by the Pt nanocrystal in (a), initiated by electron beam irradiation. (f) High magnification ADF-STEM image of the Pt nanocrystal in (e).

Figure 9 shows an ADF-STEM image of a Pt nanocrystal after extensive electron beam irradiation followed by cooling to room temperature for imaging. The hole that was generated by initial etching at high temperature is visible. The nanoparticle after extensive electron beam irradiation transformed into a multiply twinned decahedral structure (**Figure 9**b) similar to those that have been observed extensively for the coinage group metals,[33] and less frequently for the platinum group metals.[34] Analysis of the intensity from individual atomic columns (**Figure 9**c,d) show variations near the particle edge regions that indicate variations in the number of Pt atoms The particle shown in **Figure 9**, shows a symmetric 5-fold core but an overall asymmetric decahedral morphology, the energetics of which have previously been studied for Au,[35] likely due to local interaction with the edge of the MoS_2.

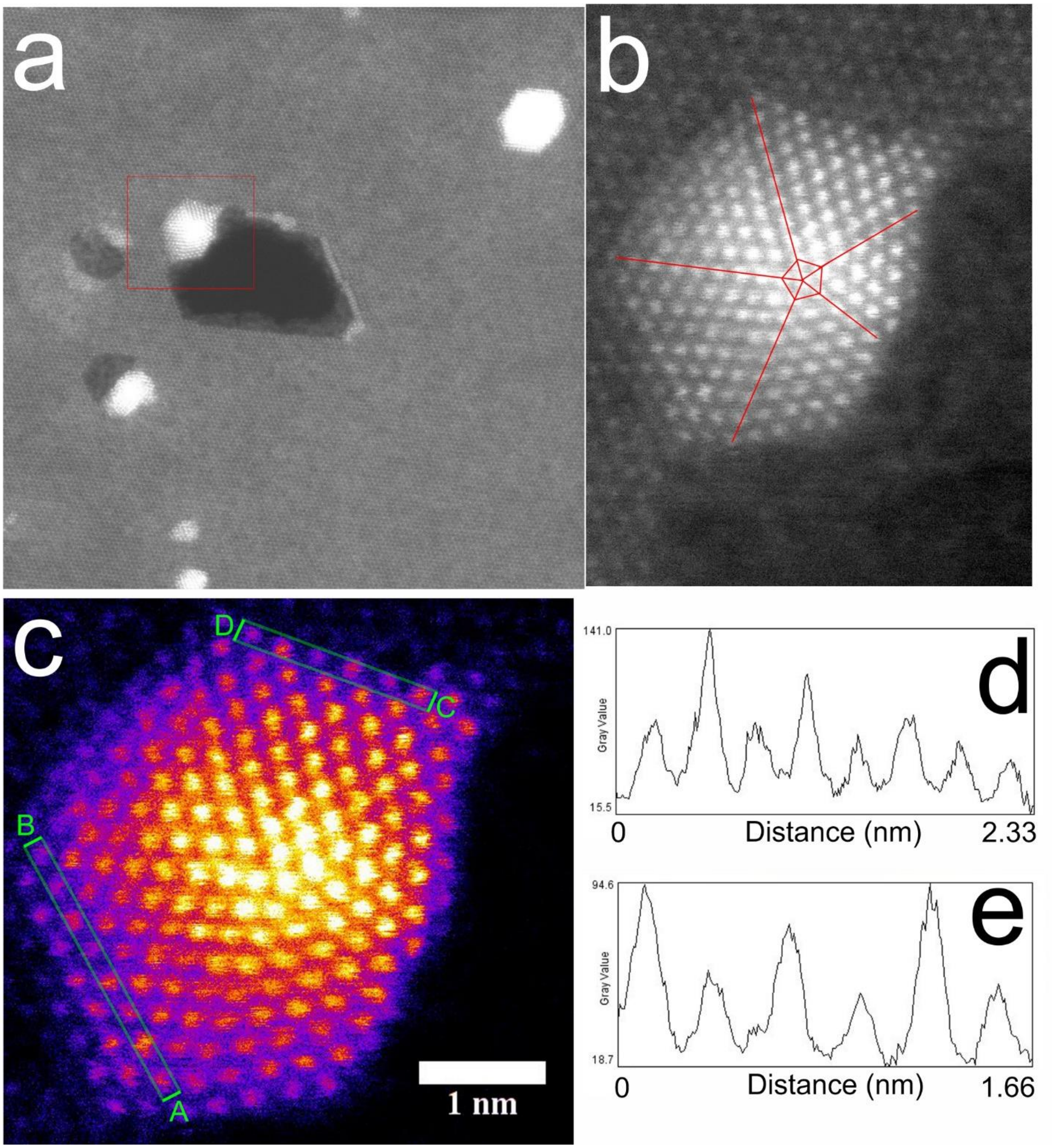

Figure 9. Nanocrystal after extensive electron beam irradiation at 800°C and then cooling to room temperature. (a) ADF-STEM image of a region where the nanocrystal has etched the MoS_2. (b) Higher magnification ADF-STEM image of the region corresponding to the red box in (a) with {11} twin planes indicates. (c) ADF-STEM image of the nanocrystal in (b), but with false colour

(‘fire’ LUT) to highlight the differences in atomic number within columns at the edge. (d) Line profile from A to B, as indicated in (c). (e) Line profile taken from C to D, as indicated in (c).

To show that the etching observed in **Figure 7** and **Figure 8** is associated with high temperature effects, we have compared the behaviour of Pt nanocrystals at room temperature (**Figure 10**). Etching of the MoS_2 lattice by the Pt nanoparticles rarely occurred and instead amorphous carbon accumulated around the Pt nanoparticles (**Figure 10**a-c). Similar carbon accumulation occurs around a single Pt atom on the surface of clean MoS_2 (**Figure 10**d-g) during electron beam irradiation. This is similar to previous reports of carbon attachment to Au atoms on MoS_2.[29] The line profile taken across this region (**Figure 10**h) shows an increased background level from the carbon accumulation. **Figure 10**i,j show the same Pt nanoparticle before and after five consecutive STEM scans and no etching is observed. This is in contrast to the temperature dependence of chemical etching seen in the defect production in 2D materials, where high temperatures reduce the electron beam induced degradation of these materials due to a reduction in the interaction between the 2D surface and gas phase ions.[36]

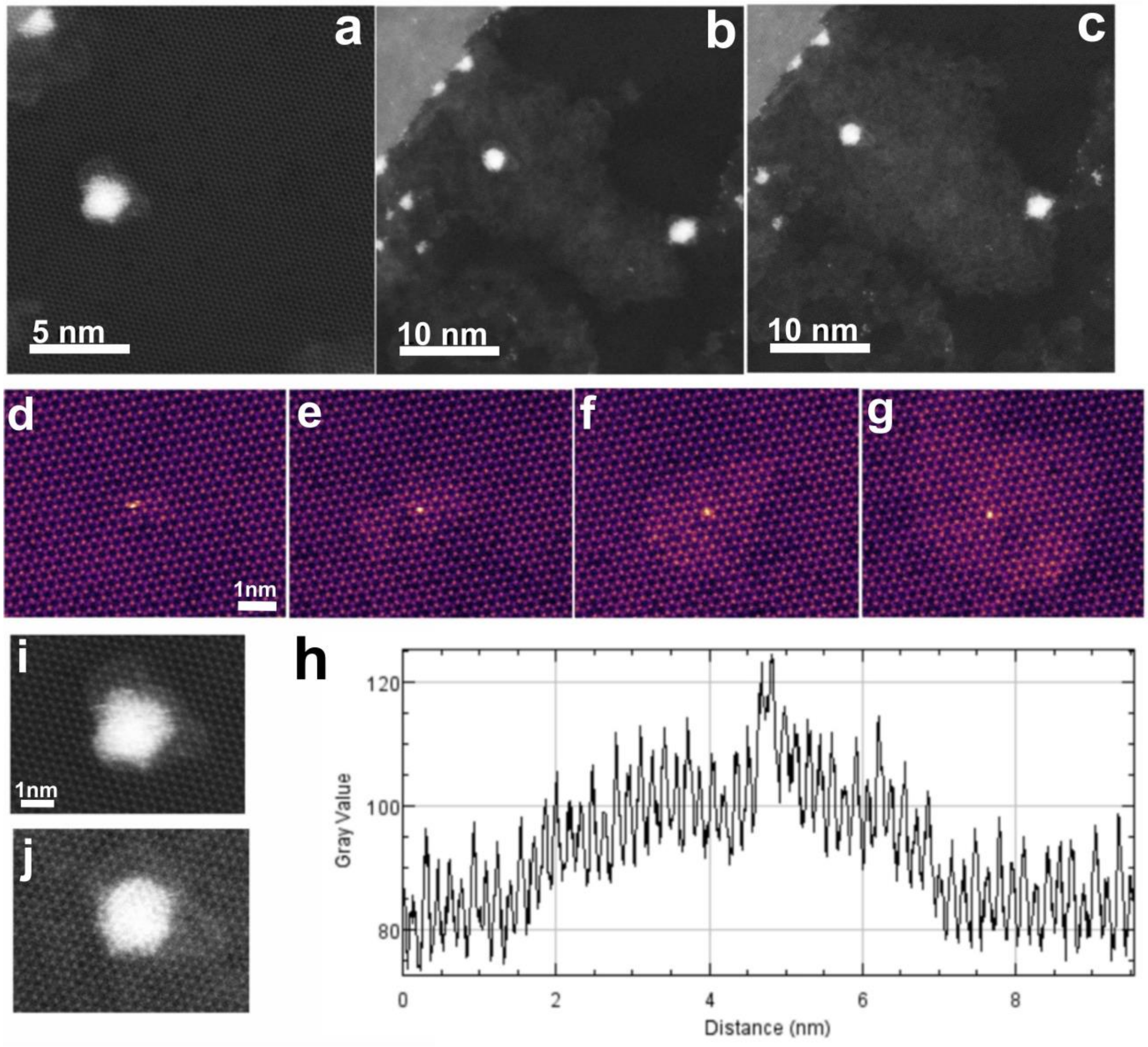

Figure 10. Room temperature imaging of Pt atoms and nanocrystals after heating to 800^{o}C and then cooling. (a) Initial ADF-STEM image of an isolated Pt nanocrystal on MoS_2. (b) and (c) ADF-STEM images after several scans (x2 for (b) and x4 for (c)) of the Pt nanoparticle in (a) showing accumulation of amorphous carbon and a lack of etching. (d)-(g) Series of ADF-STEM images of a single Pt atom on the surface of clean MoS_2 showing the accumulation of carbon around the Pt atom. (h) Line profile taken across the Pt atom with carbon accumulation in (f) showing an increased background signal due to the carbon material. (i) and (j) ADF-STEM images of the same

Pt nanocrystal before and after 5 consecutive scans, showing no sign of etching as observed at high temperature.

Conclusions

The ability to form Pt nanocrystals on the surface of MoS_2 by *in-situ* heating within the TEM enables the study of these materials without requirement for *ex-situ* cooling and re-heating. The Pt nanocrystals predominantly have two types of well-defined epitaxial correlations with the underlying MoS_2, leading (111) or (002) plane of Pt to be aligned with zigzag or armchair direction of MoS_2, respectively. For those ultrasmall Pt nanoclusters composed of ~20 atomic columns in projection, their d-spacing of (111) plane has an obvious expansion of 7-10% compared with bulk Pt, moving closer to the MoS_2 zigzag lattice spacing, which indicates a strong impact from the rigid MoS_2 template on the lattice structure of the ductile, ultrathin Pt nanocrystal. The thickness of the ultrasmall Pt nanocrystal is two-atom-thick, having only single Pt atom in each atomic column due to the non-planar structure of the FCC-Pt. Local etching of MoS_2 by the Pt nanocrystals occurs during the heating process and the *in-situ* observations initiated by the electron beam indicate that Mo atoms can be incorporated into these clusters during this process. The similarity in Mo and Pt atomic radii leads to minimal changes in the FCC crystal packing of the Pt nanocrystal and is therefore hard to detect. However, given the large change in nanoparticle size after etching along with the loss of Mo from the MoS_2 lattice, it is highly likely that the Mo is alloyed with Pt in the nanocrystals. The epitaxy between the Pt and MoS_2 is maintained during etching and also after the Pt nanoparticles detach from the MoS_2 and are supported only by the carbon layer. The presence of carbon in all regions containing Pt, even at the high temperatures indicates the need to consider its role in these catalytic systems. MoS_2 (without Pt precursor deposition) normally contains carbon surface contamination from the transfer process, but when heated to 800°C this is removed. In the examples shown, the carbon is persistent at high temperatures indicating possible increased graphitization, likely due to the interactions with the Pt nanocrystals. Graphene has been grown on Pt foils by vapour deposition,[37,38] and recent work has showed how graphene shells can be formed around Pt nanocrystals during CVD growth.[39] The etching of MoS_2 by the Pt nanocrystals leads to an increased density of edge sites in the MoS_2, which are known to be active for hydrogen evolution and the holes between MoS_2 domains contain Pt nanocrystals supported by carbon. This structure may lead to interesting catalytic performance by combining edge rich MoS_2 and Pt nanocrystals and will be the subject of future investigations.

The observation of strong epitaxial alignment between the Pt and MoS_2 may also be important for electronic applications where Pt metal electrodes are used to make contact to monolayer transition metal dichalcogenides. The long range alignment of Pt clusters may enable large single crystal regions within Pt films on the MoS_2 surface that could give rise to improved current injection.

Methods

Synthesis and Transfer of Monolayer MoS_2

MoS_2 monolayers were synthesized by a hydrogen-free CVD method using molybdenum trioxide (MoO_3, $\geqslant$99.5%, Sigma-Aldrich) and sulphur (S, $\geqslant$99.5%, Sigma-Aldrich) powder as precursors, as reported previously.[40] The growth was conducted under atmospheric pressure with the carrier gas of argon and SiO_2/Si (300 nm thick SiO_2) chips were used as substrates. To avoid cross-contamination between MoO_3 and S during the reaction, an inner tube with a smaller diameter was applied to load MoO_3, which separated it from the S powder placed in the outer 1-inch quartz tube. Two furnaces were used to give a better temperature control of both precursors and the substrate. The typical heating temperature for S, MoO_3 and SiO_2/Si substrate were set to be ~ 180, ~300, and

~800 ^{0}C, respectively. After growth, monolayer MoS_2 was transferred onto an *in-situ* heating chip (DENS Solutions DENS-C-30). The surface of the $MoS_2/SiO_2/Si$ substrate was first spin-coated with a thin film of poly (methyl methacrylate) (PMMA). The specimen was then floating on a 1 mol/L potassium hydroxide (KOH) solution to etch the SiO_2. Once the PMMA/MoS_2 film was detached from the Si substrate, it was transferred to deionized water several times to remove residuals left by the etchant. Subsequently, the PMMA/MoS_2 film was transferred onto a prefabricated *in-situ* heating chip, air-dried for overnight and baked at 180 ^{0}C for 15 minutes. The PMMA scaffold was finally removed by submerging the TEM grid in acetone for 8 hours.

Deposition of Pt-based Precursor on Monolayer MoS_2

After transferring MoS_2 single layers to the *in-situ* heating chip, ~15μL of 0.025mol/L hexachloroplatinic acid (H_2PtCl_6)-ethanol solution was deposited onto the MoS_2 surface and dried in air naturally at room temperature.

Scanning Transmission Electron Microscopy with an in-situ Heating Holder and Image Processing

ADF-STEM imaging was conducted using an aberration corrected JEOL ARM300CF STEM equipped with a JEOL ETA corrector[41] operated at an accelerating voltage of 60 kV located in the electron Physical Sciences Imaging Centre (ePSIC) at Diamond Light Source. Dwell times of 5−20 μs and a pixel size of 0.006 nm px^{-1} were typically used for imaging. Optical conditions used a CL aperture of 30 μm, a convergence semi-angle of 31.5 mrad, a beam current of 44 pA, and inner-outer acquisition angles of 49.5−198 mrad. ADF-STEM imaging at high temperatures up to 800 °C was performed using a commercially available *in-situ* heating holder from DENS Solutions (SH30-4M-FS). The resistance of the platinum coil in the heating chip (DENS Solutions DENS-

C-30) is monitored in a four-point configuration, and the temperature is calculated using the Callendar−Van Dusen equation (with calibration constants provided by the manufacturer). Slits were produced into the Si_3N_4 membranes focused ion beam milling before transferring monolayer MoS_2 onto the heating chip. Images were processed using the ImageJ software. A fire false colour LUT was applied to grayscale images to improve the visual effect.

Conflict of Interest: The authors declare no competing financial interest.

Acknowledgements

JHW thanks the Royal Society for support. SW thanks the China Scholarship Council for support. AIK acknowledges EPSRC support under platform grant EP/K032518/1.

References

(1) Turner, J. A. Sustainable Hydrogen Production. *Science* **2004**, *305*, 972–974.

(2) Subbaraman, R.; Tripkovic, D.; Chang, K.-C.; Strmcnik, D.; Paulikas, A. P.; Hirunsit, P.; Chan, M.; Greeley, J.; Stamenkovic, V.; Markovic, N. M. Trends in Activity for the Water Electrolyser Reactions on 3d M(Ni,Co,Fe,Mn) Hydr(oxy)oxide Catalysts. *Nat. Mater.* **2012**, *11*, 550–557.

(3) Subbaraman, R.; Tripkovic, D.; Strmcnik, D.; Chang, K. C.; Uchimura, M.; Paulikas, A. P.; Stamenkovic, V.; Markovic, N. M. Enhancing Hydrogen Evolution Activity in Water Splitting by Tailoring Li^+-$Ni(OH)_2$-Pt Interfaces. *Science* **2011**, *334*, 1256–1260.

(4) Nørskov, J. K.; Bligaard, T.; Logadottir, A.; Kitchin, J. R.; Chen, J. G.; Pandelov, S.; Stimming, U. Trends in the Exchange Current for Hydrogen Evolution. *J. Electrochem. Soc.* **2005**, *152*, J23–J26.

(5) Cheng, N.; Stambula, S.; Wang, D.; Banis, M. N.; Riese, A.; Xiao, B.; Li, R.; Sham, T.-K.; Liu, L.; Botton, G. A.; Sun; X. Platinum Single Atom and Cluster Catalysis of the Hydrogen Evolution Reaction. *Nat. Commun.* **2016**, *7*, 13638.

(6) Yin, H.; Zhao, S.; Zhao, K.; Muqsit, A.; Tang, H.; Chang, L.; Zhao, H.; Gao, Y.; Tang, Z. Ultrathin Platinum Nanowires Grown on Single-Layered Nickel Hydroxide with High Hydrogen Evolution Activity. *Nat. Commun.* **2015**, *6*, 6430.

(7) Li, H.; Tsai, C.; Koh, A. L.; Cai, L.; Contryman, A. W.; Fragapane, A. H.; Zhao, J.; Han, H. S.; Manoharan, H. C.; Abild-Pedersen, F.; Nørskov, J. K.; Zheng, X. Activating and Optimizing MoS2 Basal Planes for Hydrogen Evolution through the Formation of Strained Sulphur Vacancies. *Nat. Mater.* **2015**, *15*, 48–53.

(8) Merki, D.; Hu, X. Recent Developments of Molybdenum and Tungsten Sulfides as Hydrogen Evolution Catalysts. *Energy Environ. Sci.* **2011**, *4*, 3878–3888.

(9) Ye, G.; Gong, Y.; Lin, J.; Li, B.; He, Y.; Pantelides, S. T.; Zhou, W.; Vajtai, R.; Ajayan, P. M. Defects Engineered Monolayer MoS_2 for Improved Hydrogen Evolution Reaction. *Nano Lett.* **2016**, *16*, 1097–1103.

(10) Voiry, D.; Salehi, M.; Silva, R.; Fujita, T.; Chen, M.; Asefa, T.; Shenoy, V. B.; Eda, G.; Chhowalla, M. Conducting MoS_2 Nanosheets as Catalysts for Hydrogen Evolution Reaction. *Nano Lett.* **2013**, *13*, 6222–6227.

(11) Yu, Y.; Huang, S. Y.; Li, Y.; Steinmann, S. N.; Yang, W.; Cao, L. Layer-Dependent Electrocatalysis of MoS_2 for Hydrogen Evolution. *Nano Lett.* **2014**, *14*, 553–558.

(12) Li, S.; Wang, S.; Salamone, M. M.; Robertson, A. W.; Nayak, S.; Kim, H.; Tsang, S. E.;

Pasta, M.; Warner, J. H. Edge-Enriched 2D MoS_2 Thin Films Grown by Chemical Vapor Deposition for Enhanced Catalytic Performance. *ACS Catal.* **2017**, *7*, 877–886.

(13) Shi, J.; Ma, D.; Han, G.-F.; Zhang, Y.; Ji, Q.; Gao, T.; Sun, J.; Song, X.; Li, C.; Zhang, Y.; Liu, Z. Controllable Growth and Transfer of Monolayer MoS_2 on Au Foils and Its Potential Application in Hydrogen Evolution Reaction. *ACS Nano* **2014**, *8*, 10196–10204.

(14) Deng, J.; Li, H.; Xiao, J.; Tu, Y.; Deng, D.; Yang, H.; Tian, H.; Li, J.; Ren, P.; Bao, X. Triggering the Electrocatalytic Hydrogen Evolution Activity of Inert Two-Dimensional MoS_2 Surface *via* Single-Atom Metal Doping. *Energy Environ. Sci.* **2015**, *8*, 1594–1601.

(15) Deng, D.; Novoselov, K. S.; Fu, Q.; Zheng, N.; Tian, Z.; Bao, X. Catalysis with Two-Dimensional Materials and Their Heterostructures. *Nat. Nanotechnol.* **2016**, *11*, 218–230.

(16) Huang, X.; Zeng, Z.; Bao, S.; Wang, M.; Qi, X.; Fan, Z.; Zhang, H. Solution-Phase Epitaxial Growth of Noble Metal Nanostructures on Dispersible Single-Layer Molybdenum Disulfide Nanosheets. *Nat. Commun.* **2013**, *4*, 1444.

(17) Warner, J. H.; Margine, E. R.; Mukai, M.; Robertson, A. W.; Giustino, F.; Kirkland, A. I. Dislocation-Driven Deformations in Graphene. *Science* **2012**, *337*, 209–212.

(18) Wang, S.; Lee, G.-D.; Lee, S.; Yoon, E.; Warner, J. H. Detailed Atomic Reconstruction of Extended Line Defects in Monolayer MoS_2. *ACS Nano* **2016**, *10*, 5419–5430.

(19) Wang, S.; Qin, Z.; Jung, G. S.; Martin-martinez, F. J.; Buehler, M. J.; Warner, J. H. Atomically Sharp Crack Tips in Monolayer MoS_2 and Their Enhanced Toughness by Vacancy Defects. *ACS Nano* **2016**, *10*, 9831–9839.

(20) Chen, Q.; He, K.; Robertson, A. W.; Kirkland, A. I.; Warner, J. H. Atomic Structure and

Dynamics of Epitaxial 2D Crystalline Gold on Graphene at Elevated Temperatures. *ACS Nano* **2016**, *10*, 10418–10427.

(21) Gong, C.; Robertson, A. W.; He, K.; Lee, G.; Yoon, E.; Allen, C. S.; Kirkland, A. I.; Warner, J. H. Thermally Induced Dynamics of Dislocations in Graphene at Atomic Resolution. *ACS Nano* **2015**, *9*, 10066–10075.

(22) Gong, C.; He, K.; Chen, Q.; Robertson, A. W.; Warner, J. H. *In Situ* High Temperature Atomic Level Studies of Large Closed Grain Boundary Loops in Graphene. *ACS Nano* **2016**, *10*, 9165–9173.

(23) Krivanek, O. L.; Chisholm, M. F.; Nicolosi, V.; Pennycook, T. J.; Corbin, G. J.; Dellby, N.; Murfitt, M. F.; Own, C. S.; Szilagyi, Z. S.; Oxley, M. P.; Pantelides, S. T.; Pennycook, S. J. Atom-by-Atom Structural and Chemical Analysis by Annular Dark-Field Electron Microscopy. *Nature* **2010**, *464*, 571–574.

(24) Warner, J. H.; Lin, Y.; He, K.; Koshino, M.; Suenaga, K. Stability and Spectroscopy of Single Nitrogen Dopants in Graphene at Elevated Temperatures. *ACS Nano* **2014**, *8*, 11806–11815.

(25) Lin, Y.-C.; Dumcenco, D. O.; Huang, Y.-S.; Suenaga, K. Atomic Mechanism of the Semiconducting-to-Metallic Phase Transition in Single-Layered MoS_2. *Nat. Nanotechnol.* **2014**, *9*, 391–396.

(26) Zhou, W.; Zou, X.; Najmaei, S.; Liu, Z.; Shi, Y.; Kong, J.; Lou, J.; Ajayan, P. M.; Yakobson, B. I.; Idrobo, J.-C. Intrinsic Structural Defects in Monolayer Molybdenum Disulfide. *Nano Lett.* **2013**, *13*, 2615–2622.

(27) Li, H.; Wang, S.; Samuels, T.; Ggoch, G.; Han, D.; Allen, C. S.; Kirkland, A. I.; Grossman, J. C.; Jamie, H. Atomic Structure and Dynamics of Single Pt Atom Interactions with Monolayer MoS_2. *ACS Nano* **2017**, *11*, 3392–3403.

(28) Robertson, A. W.; Lin, Y.; Wang, S.; Sawada, H.; Allen, C. S.; Chen, Q.; Lee, S.; Lee, G.; Han, S.; Yoon, E.; Kirkland, A. I.; Kim, H.; Suenaga, K.; Warner, J. H. Atomic Structure and Spectroscopy of Single Metal (Cr, V) Substitutional Dopants in Monolayer MoS_2. *ACS Nano* **2016**, *10*, 10227–10236.

(29) Lin, Y. C.; Dumcenco, D. O.; Komsa, H.-P.; Niimi, Y.; Krasheninnikov, A. V.; Huang, Y.-S.; Suenaga, K. Properties of Individual Dopant Atoms in Single-Layer MoS_2: Atomic Structure, Migration, and Enhanced Reactivity. *Adv. Mater.* **2014**, *26*, 2857–2861.

(30) Zan, R.; Bangert, U.; Ramasse, Q.; Novoselov, K. S. Interaction of Metals with Suspended Graphene Observed by Transmission Electron Microscopy. *J. Phys. Chem. Lett.* **2012**, *3*, 953–958.

(31) Zhang, K.; Feng, S.; Wang, J.; Azcatl, A.; Lu, N.; Addou, R.; Wang, N.; Zhou, C.; Lerach, J.; Bojan, V.; Kim, M. J.; Chen, L.-Q.; Wallace, R. M.; Terrones, M.; Zhu, J.; Robinson, J. A. Manganese Doping of Monolayer MoS_2: The Substrate Is Critical. *Nano Lett.* **2015**, *15*, 6586–6591.

(32) Wang, S.; Li, H.; Zhang, J.; Guo, S.; Xu, W.; Grossman, J. C.; Warner, J. H. Epitaxial Templating of Two-Dimensional Metal Chloride Nanocrystals on Monolayer Molybdenum Disulfide. *ACS Nano* **2017**, *11*, 6404–6415.

(33) Marks, L. D.; Peng, L. Nanoparticle Shape, Thermodynamics and Kinetics. *J. Phys. Condens. Matter* **2016**, *28*, 53001.

(34) Duff, D. G.; Edwards, P. P.; Evans, J.; Gauntlett, J. T.; Jefferson, D. A.; Johnson, B. F. G.; Kirkland, A. I.; Smith, D. J. A Joint Structural Characterisation of Colloidal Platinum by EXAFS and HREM. *Angew. Chem. Int. Ed. Engl.* **1989**, *28*, 590–593.

(35) Uppenbrink, J.; Wales, D. J.; Kirkland, A. I.; Jefferson, D. A.; Urban, J. Structure and Energetics of Model Symmetric and Asymmetric Decahedra. *Philos. Mag. B* **1992**, *65*, 1079–1096.

(36) He, K.; Robertson, A. W.; Fan, Y.; Allen, C. S.; Lin, Y.-C.; Suenaga, K.; Kirkland, A. I.; Warner, J. H. Temperature Dependence of the Reconstruction of Zigzag Edges in Graphene. *ACS Nano* **2015**, *9*, 4786–4795.

(37) Sutter, P.; Sadowski, J. T.; Sutter, E. Graphene on Pt(111): Growth and Substrate Interaction. *Phys. Rev. B* **2009**, *80*, 1–10.

(38) Gao, L.; Ren, W.; Xu, H.; Jin, L.; Wang, Z.; Ma, T.; Ma, L.-P.; Zhang, Z.; Fu, Q.; Peng, L.-M.; Bao, X.; Cheng, H.-M. Repeated Growth and Bubbling Transfer of Graphene with Millimetre-Size Single-Crystal Grains Using Platinum. *Nat. Commun.* **2012**, *3*, 699.

(39) Kim, H.; Robertson, A. W.; Kim, S. O.; Kim, J. M.; Warner, J. H. Resilient High Catalytic Performance of Platinum Nanocatalysts with Porous Graphene Envelope. *ACS Nano* **2015**, *9*, 5947–5957.

(40) Wang, S.; Wang, X.; Warner, J. H. All Chemical Vapor Deposition Growth of MoS_2:h-BN Vertical van Der Waals Heterostructures. *ACS Nano* **2015**, *9*, 5246–5254.

(41) Hosokawa, F.; Sawada, H.; Kondo, Y.; Takayanagi, K.; Suenaga, K. Development of Cs and Cc Correctors for Transmission Electron Microscopy. *Microscopy* **2013**, *62*, 23–41.

TOC graphic